Separation and imaging of seismic diffractions using a localized rank-reduction method with adaptively selected ranks[a]

[a]Published in Geophysics, 85, no. 6, V497-V506, (2020)

Hang Wang *, *Xingye Liu* † *and Yangkang Chen**

ABSTRACT

Seismic diffractions are some weak seismic events hidden within the more dominant reflection events in a seismic profile. Separating diffraction energy from the post-stack seismic profiles can help infer the subsurface discontinuities that generate the diffraction events. The separated seismic diffractions can be migrated with a traditional seismic imaging method or a specifically designed migration method to highlight the diffractors, i.e., the diffraction image. Traditional diffraction separation methods based on the the underlying plane-wave assumption are limited by either the inaccurate slope estimation or the plane-wave assumption of the PWD filter, and thus will cause reflection leakage into the separated diffraction profile. The leaked reflection energy will deteriorate the resolution of the subsequent diffraction imaging result. Here, we propose a new diffraction separation method based on a localized rank-reduction method. The localized rank-reduction method assumes the reflection events to be locally low-rank and the diffraction energy can be separated by a rank-reduction operation. Compared with the global rank-reduction method, the localized rank-reduction method is more constrained in selecting the rank and is free of separation artifacts. We use a carefully designed synthetic example to demonstrate that the localized rank-reduction method can help separate the diffraction energy from a post-stack seismic profile with both kinematically and dynamically accurate performance.

INTRODUCTION

Diffraction is a very common wave type that can be observed in almost every seismic data set. Small-scale geological bodies (such as faults and fractures in carbonate rocks) are the main cause. As the simple hydrocarbon reservoirs have been fully explored and exploited, the unconventional hydrocarbon reservoirs controlled by these small geological bodies are now drawing attentions of exploration geophysicists. The well-preserved diffraction can provide rich information about these reservoirs (Gelius, 1995; Landa and Keydar, 1998; Decker et al., 2017). However, in the traditional

seismic exploration workflow, diffractions are treated as a kind of noise and removed from the original data. In addition, the weakness of diffraction amplitudes leads to final imaging challenges. Thus, developing effective and accurate methods for diffraction imaging would be a beneficial goal.

Generally, the key of diffraction imaging is to accurately separate the reflection and diffraction. Based on this idea, many separating methods have been proposed , which can be divided into two main categories according to their mathematical algorithms, path-summation-based methods and wave-equation-based methods. Additionally, some other approaches such as machine learning (Tschannen et al., 2020) are also effective tools for imaging the diffraction (Protasov et al., 2019).

For the path-summation-based methods, the traveltime (event shape) is of great importance to the separation of reflection and diffraction (Kanasewich and Phadke, 1988; Santos et al., 2012). Berkovitch et al. (2009) use a multifocusing algorithm to separate diffractions from reflections by designing a novel time-correction formula to approximate the diffraction events. This method can make the energy of diffraction more focused while scattering that of reflection in the stacking result. Dell and Gajewski (2011) separate diffraction and reflection energy in the time domain using a common-reflection-surface algorithm. Different synthetic examples showed the validity of this method. Waheed et al. (2013) propose a new method for fitting the diffraction traveltimes in the TI media. This approach can accelerate the traditional process for solving equation and lower the computational complexity. Additionally, it adaptively selects the best parameters for the traveltime equation without complex modeling processes. Asgedom et al. (2013) combine two novel algorithms, i.e., the modified commonreflectionsurface method and the replacementmedia technique, to enhance the weak diffraction in the strong reflection background. Coimbra et al. (2018) propose the finite-offset double-square-root diffraction traveltime equationthat can accurately separate diffraction from the background reflection. A simplified version was also proposed to accelerate the calculation of the equation parameters while keeping the quality of result unchanged. The synthetic and field data results show the outstanding performance of this improvement. Bakhtiari Rad et al. (2018) compare the influence of pre-stack and post-stack diffraction separation to imaging performance, and showed that the former method based on the wavefront attributes can help improve the illumination compared with the latter method. Li and Zhang (2019) design a vertical traveltime difference gather and its plus version. Compared with the traditional two-dimensional dip gather, this gather has the advantage of occupying less storage space. After Kirchhoff time migration, the diffraction is flattened, and the reflection events still have upward dip. By this difference, the reflection can be cut off, which will further strengthen recovered diffraction amplitudes. Merzlikin et al. (2019) introduce the separation of diffraction into an inversion framework, and designed a new decomposition algorithm by combining Kirchhoff modeling, plane-wave deconstruction and an integral operator. This method simultaneously separates weak diffraction and strong reflection accurately, while sufficiently supressing noise. Schwarz (2019) design an adaptive filter to separate diffraction in the background of strong reflection. This method is mainly based on the summation of reflection data

rather than diffraction data, and uses a variety of wavefront filters in the stacking domain to separate diffraction and reflection. Using seismic and GPR data examples, they demonstrate that this method could recover weak diffraction signals effectively.

Wave-equation-based methods take all the wavefield information into consideration (Sava et al., 2005; Yuan et al., 2019). Klokov and Fomel (2012) derive a novel analytical equation to accurately separate the diffraction and reflection. After the migration process, the Radon transform can distinguish the diffraction effectively by its shape feature. This method is very stable on both synthetic and field data examples. Zhang and Zhang (2014) image the weak diffraction in the shot and opening-angle gathers by muting the strong reflection and enhancing the weak diffraction. This method generates satisfactory results even if the diffraction interferes with the reflection. The velocities for migration can be gradually updated based on the migrated results to achieve the best result. The real and synthetic data all showed the validity of this method. Liu et al. (2016) propose a fast migration method for the imaging of diffraction. They first use linear Radon transform to obtain the local plane waves, and then implement the zero-lag correlation between these plane waves and incident waves. The final diffraction image is generated after the energy of reflected wave was attenuated by a median filter. Zhang et al. (2019) divide the wavefield into two parts, left and right, by using reverse time migration. Based on the fact that the reflection is always related to a specific dip angle, and can only exist in either the left or right wave field. However, due to the nature of diffraction, associated energy will simultaneously appear in both components at point-by-point multiplication between two components can suppress reflection while the imaging result of diffraction.

Fomel et al. (2007) proposes a two-step diffraction separation and imaging framework. The first step separates diffraction and reflection wavefields based on the spatial coherence using the plane-wave destruction (PWD) method. The PWD method assumes that the reflection waves have better spatial coherence than the diffraction waves, and thus can be predicted by neighbor traces following the smooth local slope field. In the second step, the separated diffraction waves are migrated using different velocities. Their corresponding focusing performance on the images are measured to determine the migration velocity that optimally focuses the image. In this way, one can achieve simultaneous velocity estimation and diffraction imaging. Based on this framework, the diffraction separation becomes a pure signal processing task, where no prior subsurface velocity models are required. Thus, this method is easy to apply and sometimes can obtain very good performance in real data applications. In a similar framework, Zhou et al. (2017) and Zhou and Sun (2018) develop a method to extract diffractions from high-resolution coal seismic data using localized moving-average-error filter (MAEF) to flattened reflection seismic data and or along the reflection dips based on the estimated dip by gradient calculation. However, the success of this method depends on the accuracy of the estimated slope. Because of the smoothness of the local slope, there is leakage of reflection energy into the diffraction estimate which contaminates the imaging results.

In this paper, we propose a new diffraction separation method based on a local-

ized rank-reduction method (LRR). The LRR method also uses a local plane-wave assumption, but bypasses the step of slope estimation. The compromise between the removal of diffractions and preservation of reflections is controlled by the rank in each local window. We propose an adaptive rank-selection method for each localized window to select the optimal cut-off rank that best distinguishes between reflections and diffractions. After the diffraction separation step, an migration operation is applied to obtain the migration diffraction image, e.g., by Kirchhoff migration (Fomel, 2002a), velocity continuation (Fomel, 2003).

The paper is organized as follows: we first introduce the principles of the LRR method. Then, we introduce how we adaptively select the ranks in each local window. The hybrid LRR and adaptive rank selection method is referred to as the localized rank-reduction method with adaptively chosen ranks (LRRA). Next, we use several representative examples to demonstrate the performance of the proposed diffraction separation method, and more importantly how the new method can improve the resolution and fidelity of the final image.

METHODS FOR ADAPTIVELY SEPARATING DIFFRACTIONS

The ranks or the singular (characteristic) values of the matrix data are calculated by the SVD method and are measures of the different dipping events within the matrix data (seismic data). This approach is well-known as the matrix pencil method (MPM) (Jain, 1974; Hua and Sarkar, 1991; Sarkar and Pereira, 1995). The MPM approach has been used for dispersion estimation of sonic logging data (Lang et al., 1987; Ekstrom, 1996), and assumes that the first a few characteristic values are associated with the reflection data while the rest are related to diffractions. Therefore, we can estimate or separate reflections and diffractions from recorded seismic data by matrix rank reduction or truncation. As the seismic events are not necessarily linear or follow plane wave assumption, we propose to apply the matrix rank reduction approach on windowed data to better approximate the plane-wave assumption for the reflection data. We call this method a localized rank-reduction method.

Localized rank-reduction method

Without the loss of generalization, we introduce the theory of the rank-reduction method in the case of a 3D problem. The 2D problem is just special case of the 3D problem with a single crossline trace. In the rank-reduction method, a pre-transformed matrix, e.g., the block Hankel matrix, is assumed to be of low rank. Then the goal becomes to extract the principal components of the pre-transformed matrix, i.e., the reflection signals, and separate the diffractions that usually corresponds to the inessential components due to lower spatial coherence.

Assuming that the tensor form of the input 3D seismic data is $D(x, y, t)$, the

corresponding form in frequency-space domain is obtained after Fourier transform and can be expressed as $D(x, y, f)$. For each frequency slice, we map the frequency domain data into several block Hankel matrices. This process is referred as Hankelization (Oropeza and Sacchi, 2011; Huang et al., 2016; Siahsar et al., 2017). Given a frequency f, the Hankel matrix can be constructed as

$$\mathbf{H}_i(f) = \begin{bmatrix} D(i,1,f) & D(i,2,f) & \cdots & D(i,Q_y,f) \\ D(i,2,f) & D(i,3,f) & \cdots & D(i,Q_y+1,f) \\ \vdots & \vdots & \ddots & \vdots \\ D(i,P_y,f) & D(i,P_y+1,f) & \cdots & D(i,N_y,f) \end{bmatrix}, \tag{1}$$

where the subscript i is the row and $\mathbf{H}_i(f)$ is the Hankel matrix in frequency domain corresponding to the data matrix in frequency-space domain $D(x, y, f)$. $P_y = \lfloor N_y/2 \rfloor + 1$, $Q_y = N_y - P_y + 1$ and $\lfloor \cdot \rfloor$ denotes the integer part of an input argument. N_y denotes the number of traces in the y direction.

Then, the corresponding block Hankel matrix can be inserted with equation 1

$$\mathbf{B}(f) = \begin{bmatrix} \mathbf{H}_1(f) & \mathbf{H}_2(f) & \cdots & \mathbf{H}_{Q_x}(f) \\ \mathbf{H}_2(f) & \mathbf{H}_3(f) & \cdots & \mathbf{H}_{Q_x+1}(f) \\ \vdots & \vdots & \ddots & \vdots \\ \mathbf{H}_{P_x}(f) & \mathbf{H}_{P_x+1}(f) & \cdots & \mathbf{H}_{N_x}(f) \end{bmatrix}, \tag{2}$$

where $P_x = \lfloor N_x/2 \rfloor + 1$, $Q_x = N_x - P_x + 1$. N_x denotes the number of traces in the x direction.

The rank-reduction can be achieved by minimizing the following objective function

$$\begin{aligned} \min \quad & O = \|\mathbf{B}(f) - \mathbf{L}(f)\|_F^2 \\ \text{subject to} \quad & \text{rank}(\mathbf{L}(f)) = L, \end{aligned} \tag{3}$$

where $\mathbf{L}(f)$ denotes the low-rank section corresponding to $\mathbf{B}(f)$. L denotes the optimal rank parameter. The above objective function can be conveniently minimized by the well-known singular value decomposition (SVD). Therefore, the SVD of block Hankel matrix $\mathbf{B}(f)$ can be expressed as

$$\mathbf{B}(f) = \mathbf{U}\mathbf{\Sigma}\mathbf{V}^T, \tag{4}$$

where $\mathbf{U} = [\mathbf{u}_1, \mathbf{u}_2, \cdots, \mathbf{u}_N]$ is a left singular matrix, $\mathbf{\Sigma} = [\sigma_1, \sigma_2, \cdots, \sigma_N]$ is a singular matrix and $\mathbf{V} = [\mathbf{v}_1, \mathbf{v}_2, \cdots, \mathbf{v}_N]$ is a right singular matrix. σ_i represents the ith singular value, and N represents the number of columns of $\mathbf{B}(f)$. Next, the rank-reduced matrix $\mathbf{L}(f)$ can be calculated by extracting the first L principal components, i.e.,

$$\mathbf{L}(f) = \sum_{i=1}^{L} \sigma_i \mathbf{u}_i \mathbf{v}_i^T. \tag{5}$$

Then, the solved low-rank Hankel matrix is rearranged to a vector form according to inverse Hankelization process. The rank-reduction method can be summarized as follows:

$$\begin{aligned} \mathbf{R} &= \mathcal{F}^{-1}\mathbf{T}\mathcal{F}\mathbf{D}, \\ \mathbf{T} &= \mathcal{A}\mathcal{L}\mathcal{H}, \end{aligned} \tag{6}$$

where $\mathbf{R}$ denotes the separated reflections. The separated diffractions can directly obtained by $\mathbf{D} - \mathbf{R}$. $\mathcal{F}$ and $\mathcal{F}^{-1}$ denote forward and inverse Fourier transforms.

In equation 6, filter $\mathbf{T}$ is referred to as the frequency-domain rank-reduction operator, containing the Hankelization $\mathcal{H}$, principal component extraction $\mathcal{L}$ and inverse Hankelization process $\mathcal{A}$. Because of the complexity of seismic data, the plane-wave assumption is only valid locally. Thus, it is more appropriate to apply the rank-reduction method locally, i.e., in local windows:

$$\mathbf{R} = \mathcal{W}^{-1}\mathcal{F}^{-1}\mathbf{T}\mathcal{F}\mathcal{W}\mathbf{D}, \tag{7}$$

where $\mathcal{W}$ and $\mathcal{W}^{-1}$ denote a pair of windowing and reconstruction operators.

Automatic rank selection

In order to obtain a satisfactory result, an appropriate L, referred to the rank, should be cautiously selected. A big value of L will lead to preserving all components, while a small value of the rank will cause damage on the preserved reflections by the rank-reduction filter. In the first case, negligible diffraction energy are separated. In the second case, only the most coherent wave components, e.g., horizontal waves, are preserved (Chen et al., 2017, 2019). Thus, there will be a strong mixture between the separated reflections and diffractions. Therefore, the determination of rank parameter is difficult and traditional methods that exploit distinct event slowness (Vicente and Mauricio, 2011) cannot perform well in complicated situations.

For the rank-reduction filtering, an alternative method is to adaptively and automatically select the rank parameter based on the features and complexity of the data. In the singular spectrum, the singular values of signals and noise are discrepant. The cut-off rank in singular value spectrum can indicate the separation of signal and noise energy. On this basis, we use an adaptive strategy to optimize the rank (Chen et al., 2017, 2019). At first, we define a singular value ratio (SVR):

$$m_i = \frac{\sigma_i}{\sigma_{i+1}}, i = 1, 2, \cdots, N-1, \tag{8}$$

where $\{m_i\}$ denotes the SVR sequence, and N is the length of the singular spectrum. Then, the rank L can be calculated by maximizing the SVR sequence, i.e.,

$$\hat{L} = \arg\max_i \quad m_i. \tag{9}$$

A detailed analysis of the LRRA method on the diffraction separation problem is presented in the next section. In addition, we will aslo comprehensively analyze the reliability of the adaptive rank selection strategy in accurately separating diffractions from reflection waves in the next section.

COMPARISON OF DIFFRACTION IMAGING

Synthetic test

In order to test the effective performance of the proposed localized rank-reduction method, we use a synthetic and two real data examples to show the better diffraction separation performance of the LRRA method, and compare it with the state-of-the-art PWD based method. To demonstrate the advantages of the localized-processing and automatic rank selection strategies, we compare the rank-reduction methods in different cases, considering local or global processing, and fixed or adaptive rank selection.

We first generate the reflection data from five reflection surfaces by Kirchhoff modeling (Figure 1a). Then, we generate the diffraction data from a set of diffraction points (Figure 1b). We sum the reflection and diffraction data to output the simulated zero-offset data (Figure 1c). The size of the zero-offset dataset is 800×501. The temporal sampling is 4 ms and spatial sampling is 0.02 km. Note that the same synthetic data were also used in Merzlikin et al. (2019). We show the results from the PWD method (Fomel et al., 2007) and the proposed LRRA method in Figure 2. Figures 2a and 2c compare the separated reflectionswhile Figures 2b and 2d show the separated diffractions. It is clear that the PWD method (Figures 2a and 2b) causes significantly more residual diffractions in the separated reflections than the proposed LRRA method (Figures 2c and 2d). Correspondingly, the separated diffractions of the PWD method are much weaker than those from the proposed LRRA method. We attribute the unsatisfactory performance of the PWD method to the failure in distinguishing between the reflections and diffractions in the local slope map, as plotted in Figure 3. Because the slope estimation method calculates the slope for both reflections and diffractions, it is difficult to separate them for PWD diffraction separation method that relies on the slope difference. In this test, we use a local window with 200 samples in time and 100 samples in space. The window size is chosen so as to optimize the separability of diffractionsfrom reflections. Based on this criterion, we choose the optimal window size based on a try-and-error strategy in practice. We move the window by half of the window size in each directions, meaning that the overlap between two neighbor windows are 50%. We take the automatic rank selection strategy as introduced previously so we do not need to specify the rank parameter in the LRRA method. The PWD algorithm Fomel (2002b) in this paper is a local algorithm, but does not use local windows. Fomel (2002b) avoids the use of local window strategy by designing a non-stationary dip estimation method, where the window size is substituted by the smoothing radius. Thus the only parameter

that affects the slope estimation is the smoothing radius (along time and space). A larger smoothing radius corresponds to a larger local window size, i.e., smoother, and vice versa. But the smoothing radius does not result in the same effect as the local window strategy. For example, when we increase the smoothing radius to a large level, the diffraction slope shown in Figure 3 will be weakened. But, at the same time, the accuracy of the reflection slope will deteriorate, thereby making the reflection not fully separated. In the opposite way, if the smoothing radius is smaller, like in this paper, the diffraction slope shows up, then the diffraction is not easy to be separated. So, this is the contradiction in tuning the PWD algorithm. In this paper, we use a smoothing radius of ten samples along both horizontal and vertical directions.

To compare the performance of the automatic rank selection strategy and manual rank selection strategy, we perform several try-and-error tests by specifying different ranks based on the LRR method. Figure 4a-4d shows four separated reflection sections based on the LRR method with a fixed rank of $N = [2, 3, 4, 5]$, respectively. Correspondingly, Figure 5a-5d shows four separated diffraction sections based on the LRR method with the same fixed rank as Figure 4. From Figures 4 and 5, we can find that the residual diffraction energy in the separated reflection sections gradually increases, and the reflection energy in the separated diffraction sections decreases, as the fixed rank increases from $N = 2$ to $N = 5$. All these results from the LRR method with fixed ranks appear worse than the result from the LRRA method. For example, when $N = 2$, the separated reflection section (Figure 4a) is clean and free of diffraction, but the separated diffraction contains very strong reflection energy, which will significantly deteriorate the resolution of migrated diffractors in the diffraction image. When $N = 5$ (Figure 4d), the separated diffraction section contains pure diffraction energy, but the associated reflection section contains significant diffraction energy, thus the resulted diffraction image will not be accurate. When $N = 3$ and $N = 4$, it seems that the LRR method obtains a better compromise, but is less powerful in removing the diffractions than the LRRA method. The worse performance of the LRR method with a fixed rank compared with the LRRA method with automatically selected ranks is due to the rank inconsistency problem (Zu et al., 2017), i.e., the optimal ranks in each localized processing window are different and thus a globally defined rank cannot suit each localized window. In addition to the superior perfomance, LRRA method also avoids the try-and-error process for rank selection and is more convenient to apply.

We also compare the performance of diffraction separation based on a global rank reduction (GRR) method (Oropeza and Sacchi, 2011; Chen et al., 2016; Lin et al., 2020) with different rank choices. Figures 6a-6d show a comparison of separated reflection sections using the GRR method with a fixed rank of $N = [5, 10, 16, 25]$, respectively. Figure 7 shows a comparison of separated diffraction sections using the GRR method with the same fixed ranks as Figure 6. From Figures 6 and 7, it is evident that as the rank increases, the residual diffraction energy in the separated reflection sections reduces while the diffraction sections become cleaner and cleaner in the sense of less reflection energy. The general performance of the GRR method is similar to that of the LRR method, but it is more difficult to compromise between

the cleanness and preservation of the reflection energy for the GRR method. For example, when the separated reflection section (Figure 6d) contains the same level of residual diffraction energy as the LRR method (Figure 4d), its diffraction section contains stronger reflection energy. The GRR method tends to fail because of the non-stationarity of both reflection and diffraction energy, while the GRR method is based on a global linear-event assumption (Oropeza and Sacchi, 2011). To verify the diffraction imaging performance of the better separated diffractions using the proposed LRRA method, we plot four different diffraction images in Figure 8. Figure 8a shows a ground-truth diffraction image as a reference. Figure 8b shows the migrated image of the zero-offset dataset (Figure 1c), i.e., treating both reflections and diffractions as a whole and without special handling of the diffraction energy. Figure 8b is considered as a conventional image as compared with the more advanced diffraction image. Figure 8c shows the migrated image of the separated diffractions from the PWD method, where most diffraction points are imaged well but with some blurry points at greater depths. Figure 8d shows the diffraction image using the proposed method, where all diffraction points are imaged clearly. Besides, because the separated diffraction energy of the proposed method is stronger than that of the PWD method, the resulted image has an obviously stronger amplitude of each diffraction point.

Field data tests

The first field example (Figure 9) is a stacked dataset after applying dip-moveout (DMO). The size of the dataset is 1750×401. The temporal sampling is 4 ms and spatial sampling is 0.0167 km. This dataset was also studied previously by Decker et al. (2017). Figure 10 plots a comparison of separated diffraction sections and reflection sections between the traditional PWD method and the proposed LRRA method. Figures 10a and 10b compare the separated reflections between the two methods, while Figures 10c and 10d show the corresponding diffractions. From Figures 10c and 10d, it is clear that although the separated diffraction energy of the PWD method (Figure 10c) seems to be stronger than that of the LRRA method (Figure 10d), significant reflection energy remains in the PWD result. The labels point out some areas with obvious reflection energy, indicating a serious reflection leakage phenomenon. The diffraction section separated by the LRRA method seems to be pure diffraction energy. In this test, we use a localized processing window with a size of 100 samples in time and 20 samples in space.

We then compare the migrated reflection and diffraction images using two aforementioned methods in Figure 11. The top row of Figure 11 plots the corresponding reflection images using the velocity continuation method (Fomel, 2003) for the two methods, while Figures 11c and 11d plot the diffraction images. From Figure 11, it is clear that the proposed LRRA method obtains a better diffraction image with an obviously higher resolution. Several distinct imaging areas are highlighted by the frame boxes A, B, and C. At the same time, the reflection image of the LRRA method

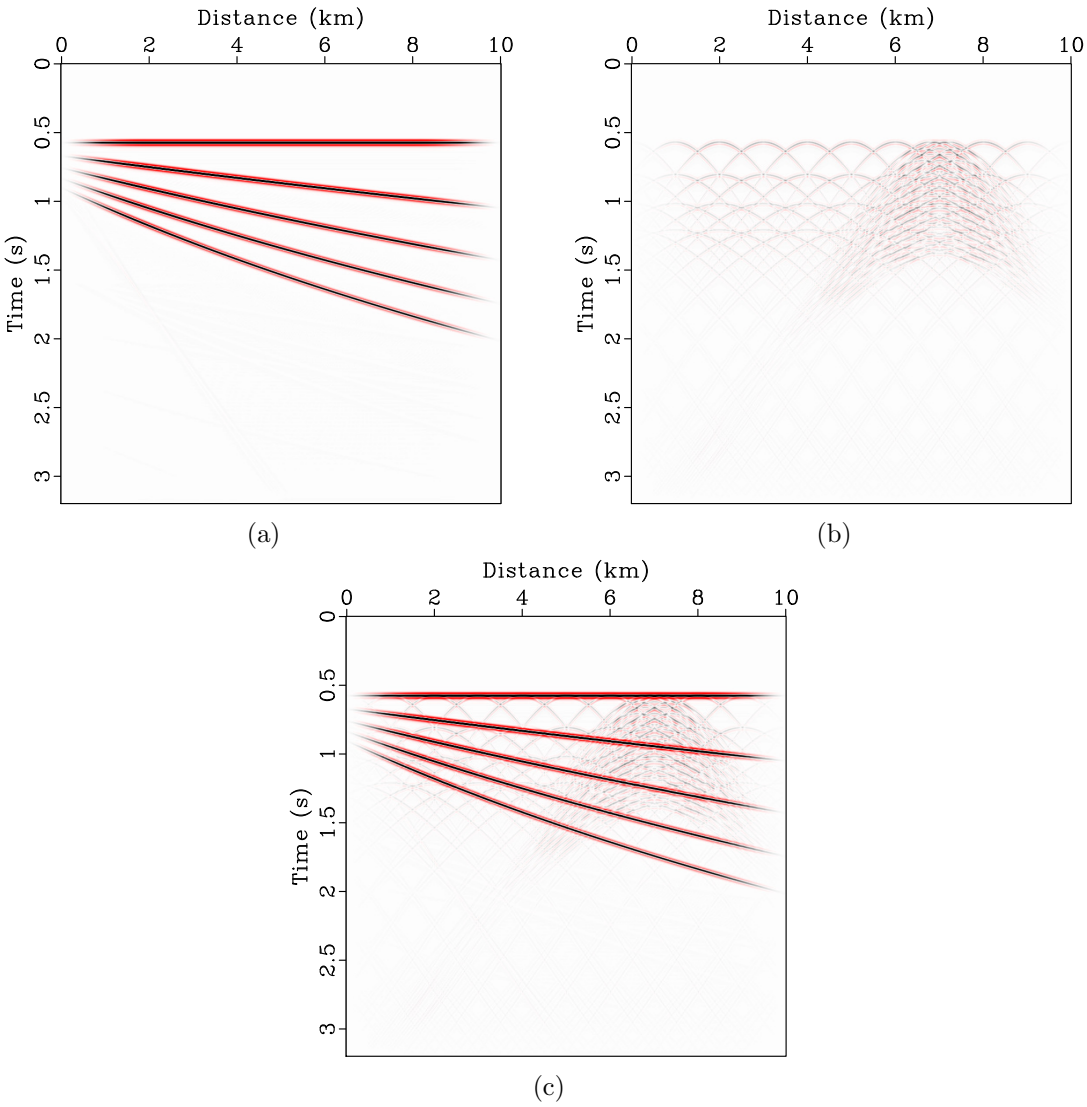

Figure 1: (a) Simulated reflection data. (b) Simulated diffraction data. (c) Simulated zero-offset data containing both reflections and diffractions.

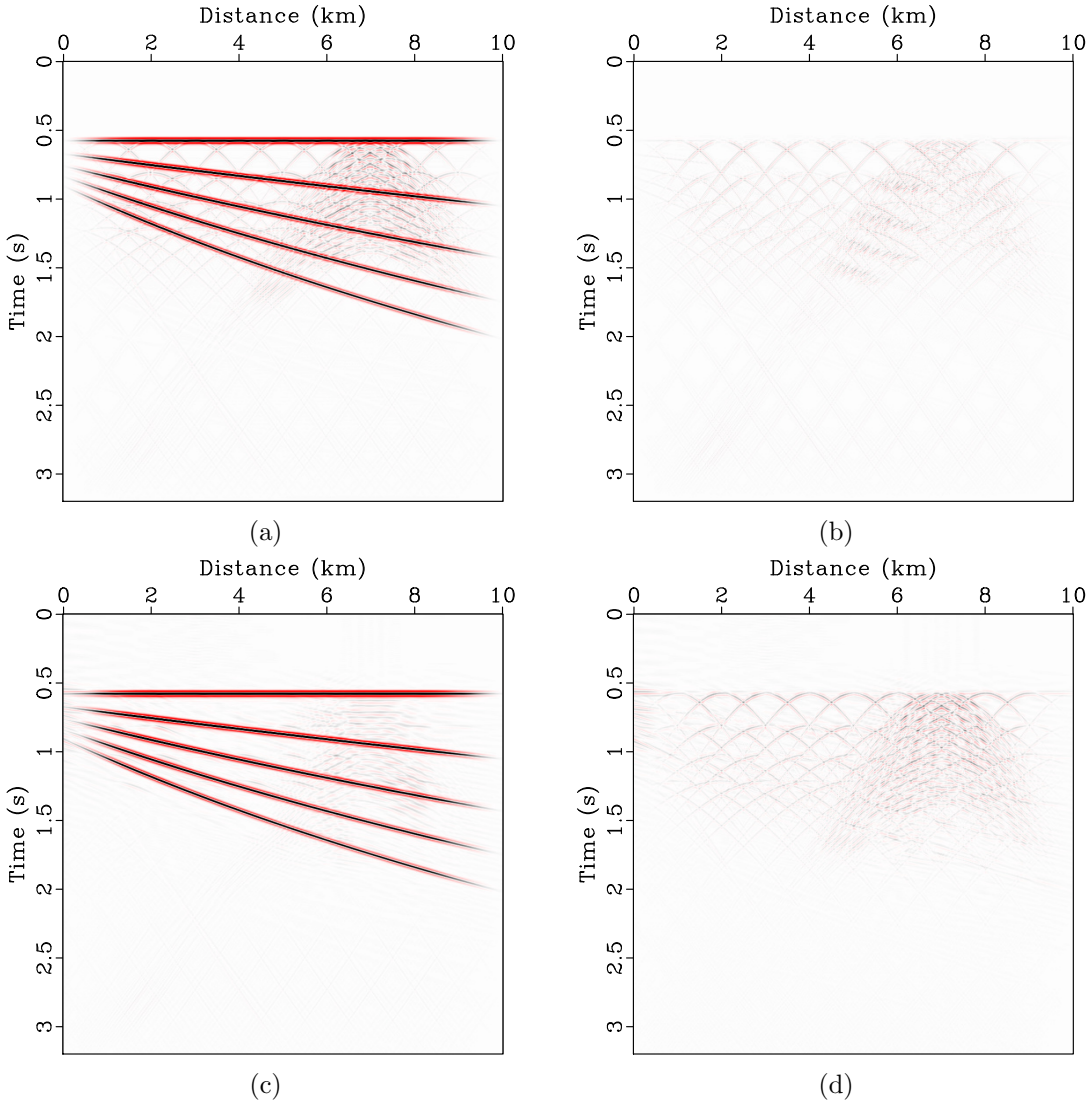

Figure 2: (a) Separated reflections using PWD method. (b) Separated diffractions using PWD method. (c) Separated reflections using LRRA method. (d) Separated diffractions using LRRA method.

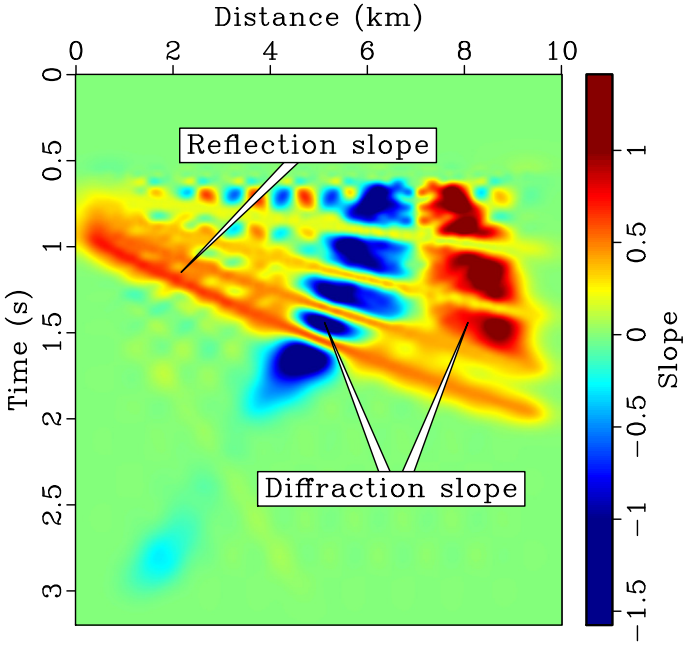

Figure 3: Estimated local slope from the zero-offset data shown in Figure 1c, which is used for PWD analysis. Note that both reflection and diffraction slopes are revealed in this map.

is more spatially continuous than the PWD method because the amplitude of reflection waves are less damaged during the diffraction separation process of the LRRA method. The migrated reflection images indicate a clear overthrust structure, with the thrust-generated faults highlighted clearly in the diffraction images. We zoom in the three areas referred to by the frame boxes and plot the zoomed sections in Figures 12 and 13. Figure 12 plots the detailed comparison of the reflection images and Figure 13 plots the comparison of the zoomed diffraction images. The top rows of Figures 12 and 13 correspond to the PWD method while the bottom rows correspond to the proposed LRRA method. These detailed comparison further confirms that the proposed LRRA method can obtain a higher resolution in the diffraction image and a better continuity in the reflection image.

We vary the fixed rank from $N = 1$ to $N = 4$ for the LRR method gradually and show their corresponding diffraction images in Figure 14. It is salient that the amplitude of diffraction images weakens as we incrase the rank, which is explained by the fact that a larger rank causes less separated diffraction energy. When $N = 1$, most discontinuities are imaged well but with very low resolution because numerous reflection structures also exist. When $N = 2$, the resolution of the diffraction image becomes higher, but it also misses a lot of significant diffraction structures, e.g., around 7.5 s. When $N > 2$, the poor diffraction quality does not provide helpful indications of the subsurface discontinuity structures. Figures 15a-15d compare the diffraction images using the GRR method with ranks of $N = [5, 10, 20, 30]$, respectively, in Figure 15.

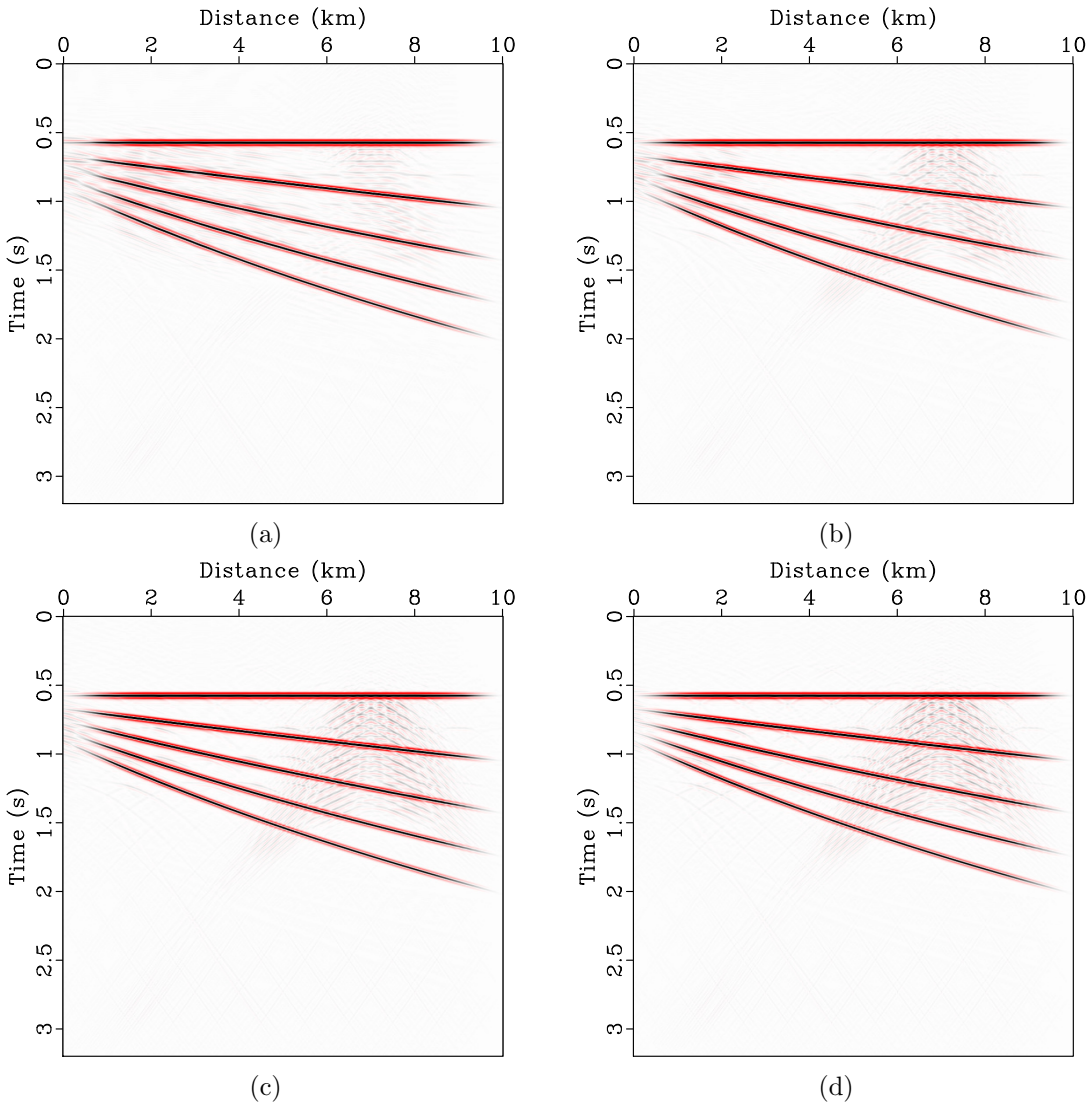

Figure 4: Separated reflections using LRR method with (a) N=2, (b) N=3, (c) N=4, (d) N=5.

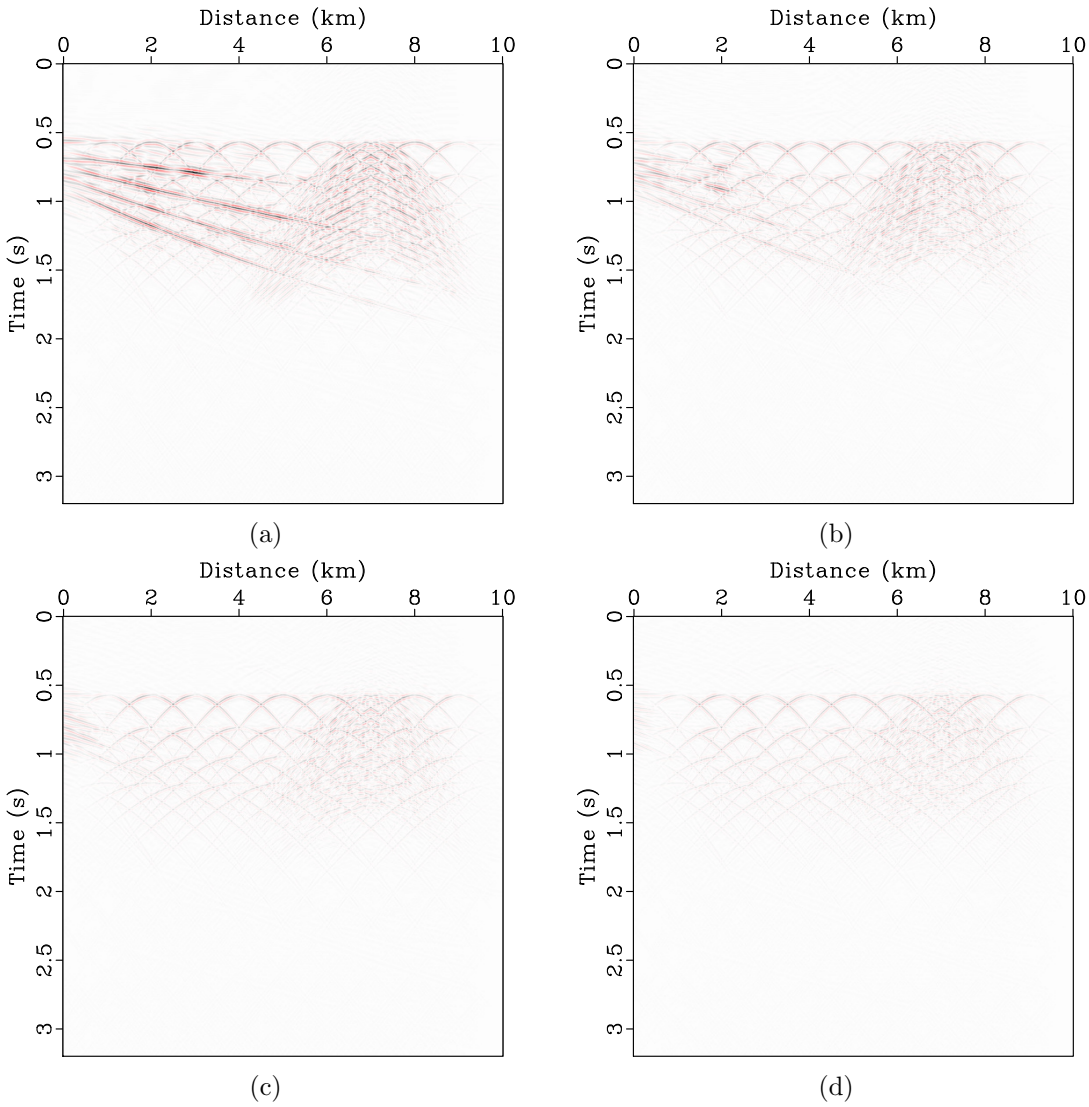

Figure 5: Separated diffractions using LRR method with (a) N=2, (b) N=3, (c) N=4, (d) N=5.

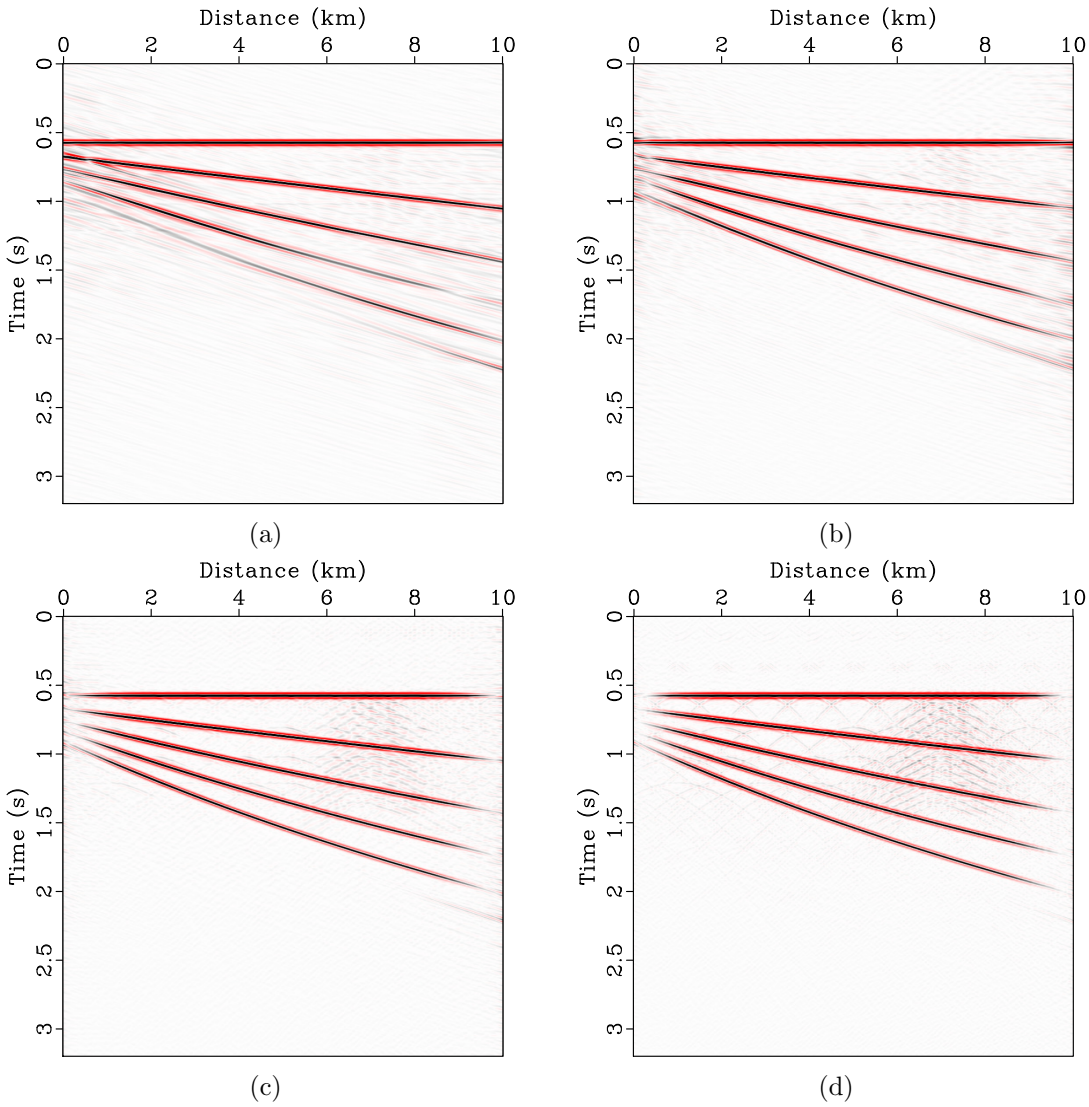

Figure 6: Separated reflections using GRR method with (a) N=5, (b) N=10, (c) N=16, (d) N=25.

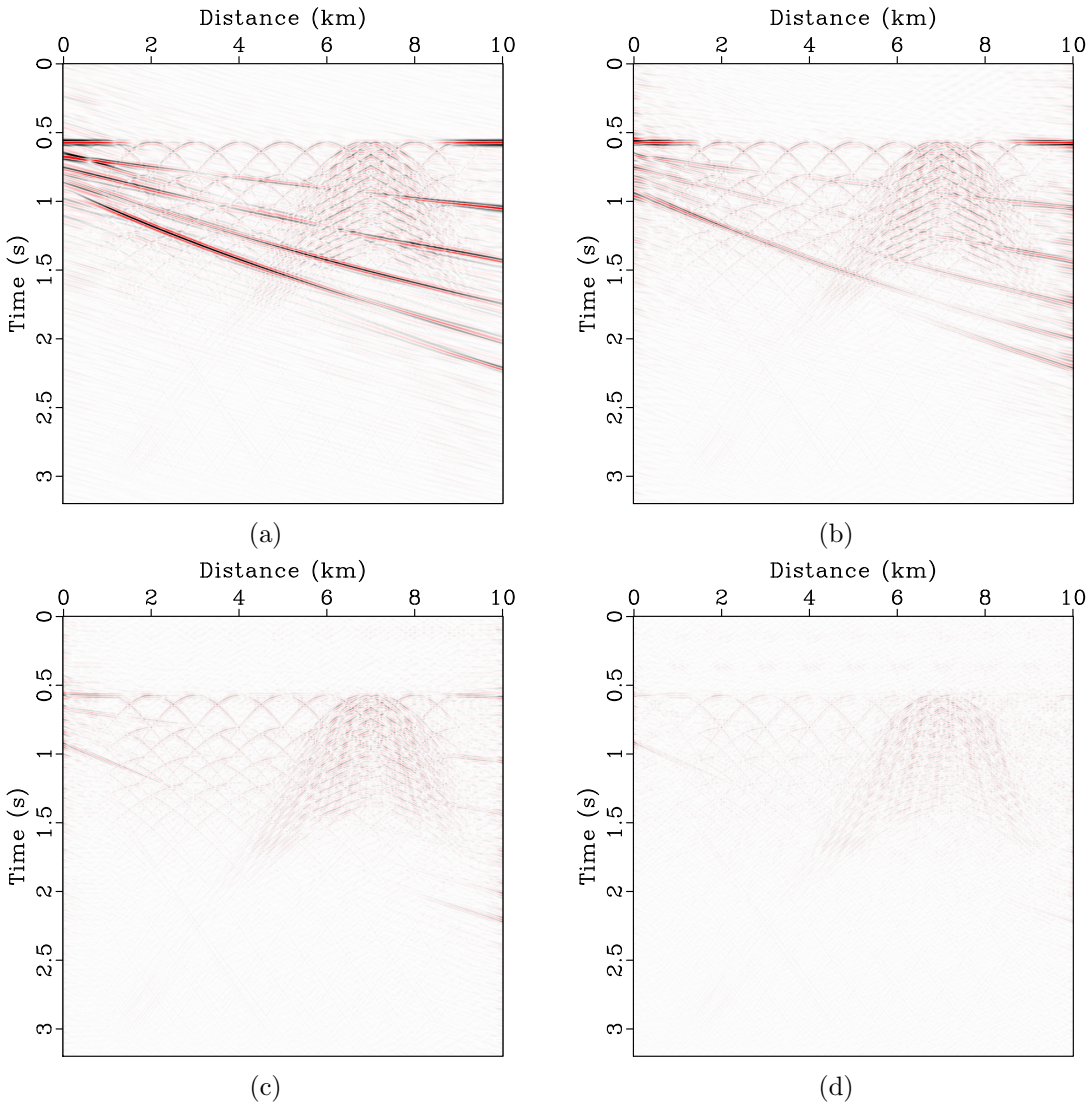

Figure 7: Separated diffractions using GRR method with (a) N=5, (b) N=10, (c) N=16, (d) N=25.

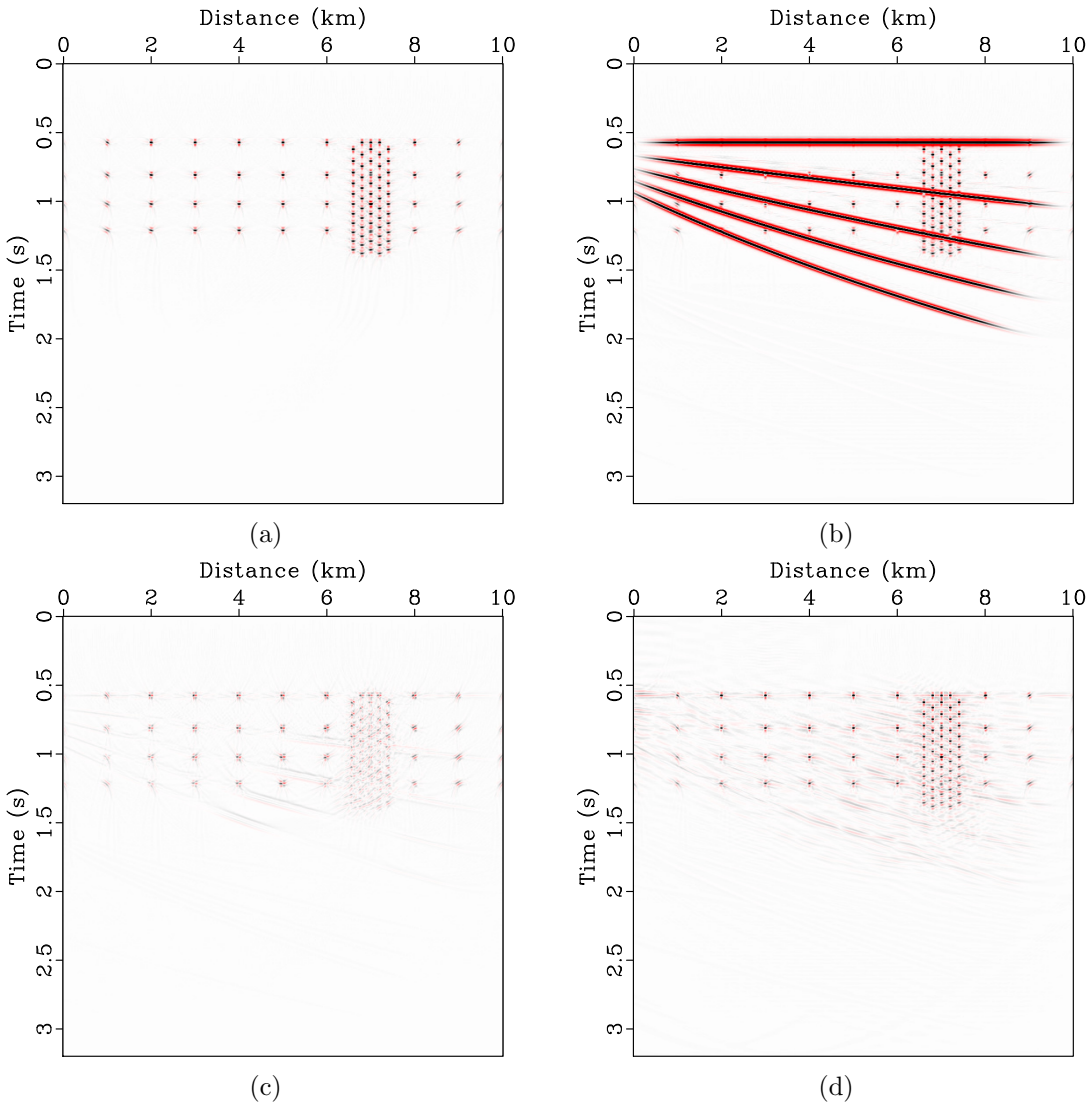

Figure 8: True diffraction image (a) and migration results of (b) traditional method, (c) PWD method, and (d) LRRA method.

It is clear that when the rank is smaller, e.g., $N \leq 10$, the diffraction images have low resolutions and more importantly contain a lot of artifacts. When the rank is larger, e.g., $N \geq 20$, the diffraction images fail to depict all the discontinuities and also contain some reflection structures. In conclusion, the GRR method is much more difficult than the LRR method in determining an appropriate compromise between resolution and completeness.

Next, we apply the proposed LRRA method to a real post-stack dataset from the Gulf of Mexico Figure 16. The post-stack seismic image of this dataset is plotted in Figure 16. There are 1000 temporal samples and 250 spatial samples in this dataset. The temporal sampling is 4 ms and the spatial sampling is 0.0335 km. We compare the separated diffraction sections using the PWD and LRRA methods in Figure 17. In this test, we use a localized window with the size of 200×50. It is clear from Figure 17 that the PWD method causes some reflection energy leakage in the separated diffractions while the LRRA method is less likely to cause the reflection leakage problem. The two frame boxes and the two labels in Figure 17 highlight some areas with distinct difference between two sections, e.g., more leaked reflection waves in the PWD result on the left. Figure 18 plots a comparison of the diffraction images using two methods, based on the velocity analysis and diffraction imaging framework introduced in Fomel et al. (2007). The comparison of diffraction images shows that the proposed LRRA method causes fewer reflection structures and a higher spatial migration resolution in the diffraction image, as indicated by the frame boxes and arrows. Figure 19 plots a comparison of the estimated velocity models by focusing the separated diffractions using the PWD method on the left and the LRRA method on the right based on the velocity continuation approach (Fomel, 2003). According to the better focused diffraction image, we consider the velocity model from the LRRA method is more accurate. However, further verification of the velocity model requires more information.

CONCLUSIONS

The diffraction separation performance of the traditional PWD filter is limited in complex geological structure, thereby causing an inaccurate slope estimation and the inadequacy of the plane-wave assumption of the PWD filter. We have proposed a new effective diffraction separation method based on the localized rank-reduction method. The rank-reduction method assumes the diffractions to be high-rank and reflections to be low-rank locally, and thus the diffraction energy can be easily separated via a simple rank-reduction filter. The localized rank-reduction method shows great advantages over the global rank-reduction method because the rank to be chosen in a localized method has a narrower range than in the global method and thus is easier to choose. More importantly, the localized rank-reduction is free of artifacts that commonly exist in global methods. The ranks of the localized rank-reduction method can be either constant or better be adaptively chosen. The adaptive rank selection strategy is simple and convenient to use. The separated diffractions and reflections based on the

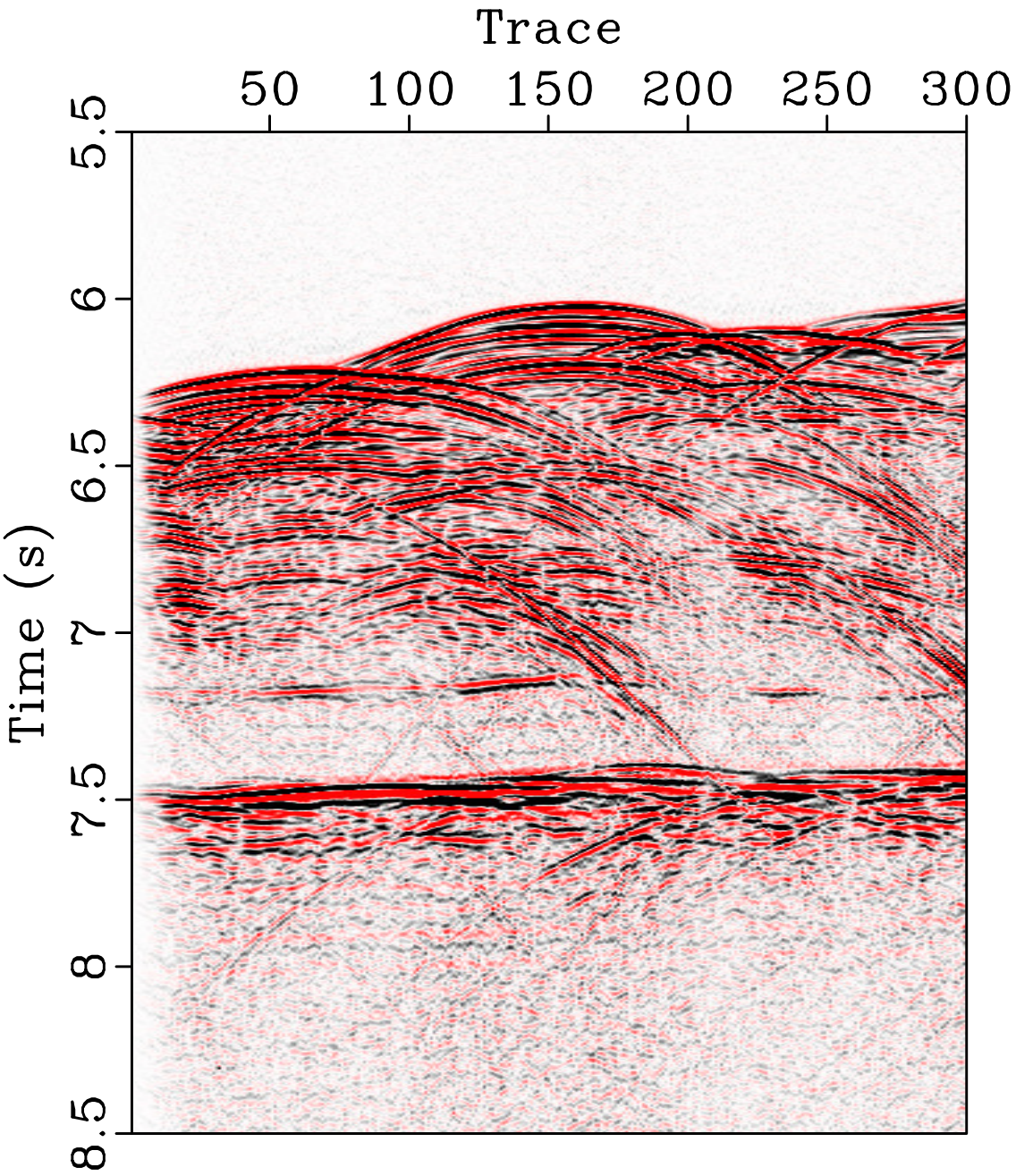

Figure 9: Input Nankai seismic data.

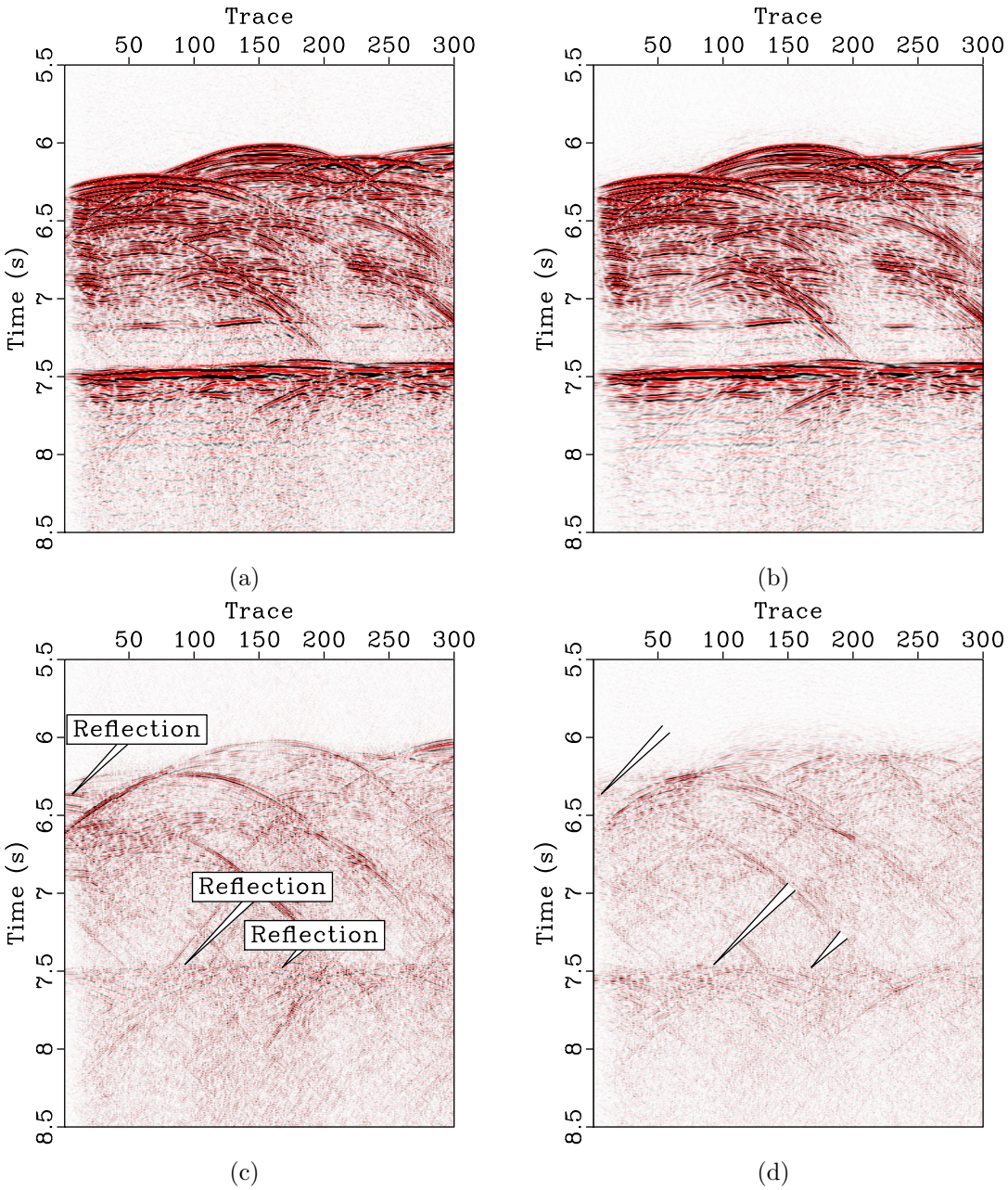

Figure 10: Separated reflection from (a) PWD method and (b) LRRA method. Separated diffraction from (c) PWD method and (d) LRRA method.

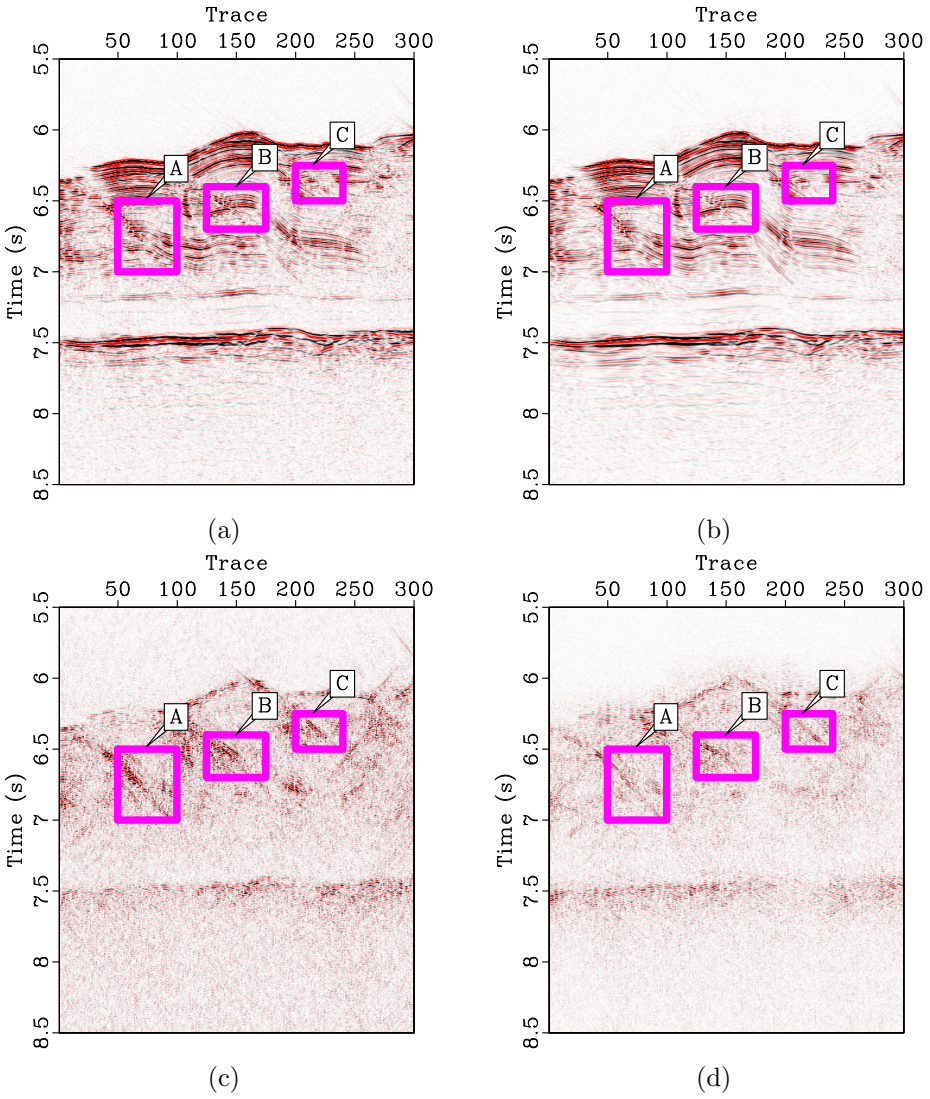

Figure 11: Comparison of diffraction and reflection images. (a) Reflection image from the PWD method. (b) Reflection image from the LRRA method. (c) Diffraction image from the PWD method. (d) Diffraction image from the LRRA method.

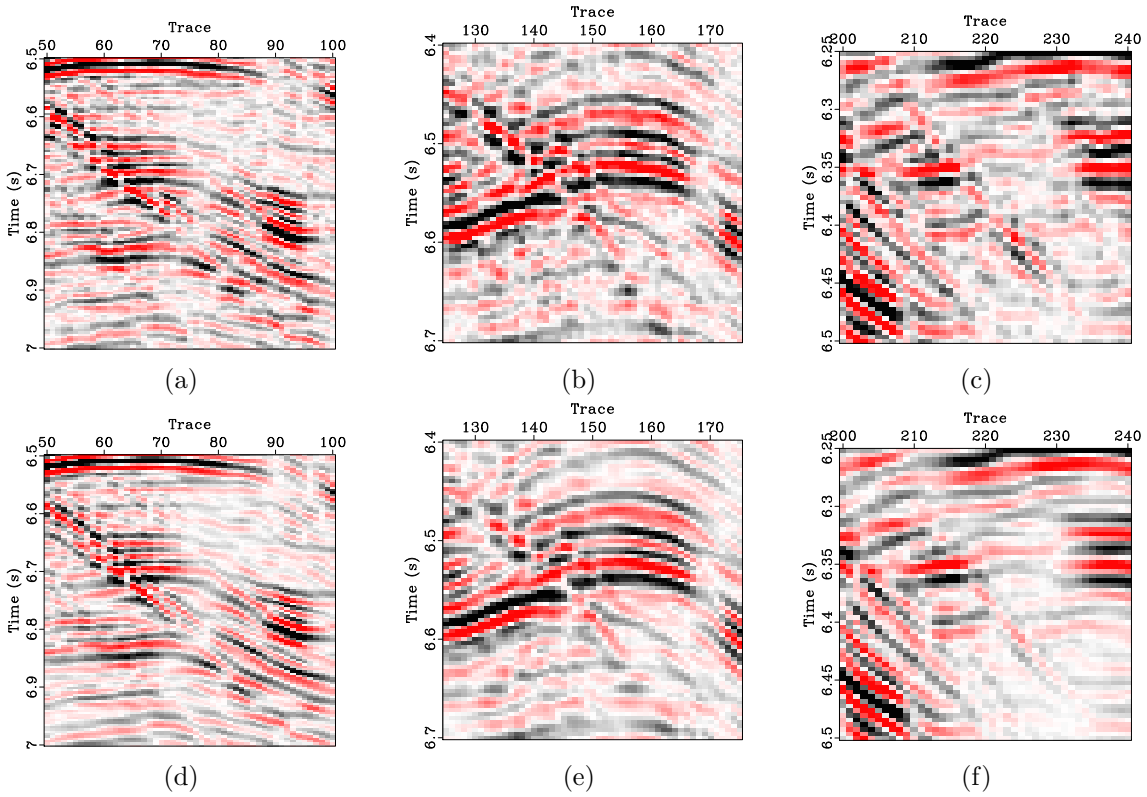

Figure 12: Zoomed comparison of the reflection image. Top row: PWD method. Bottom row: LRRA method. (a) and (d) correspond to the frame box A in Figure 11. (b) and (e) correspond to the frame box B in Figure 11. (c) and (f) correspond to the frame box C in Figure 11.

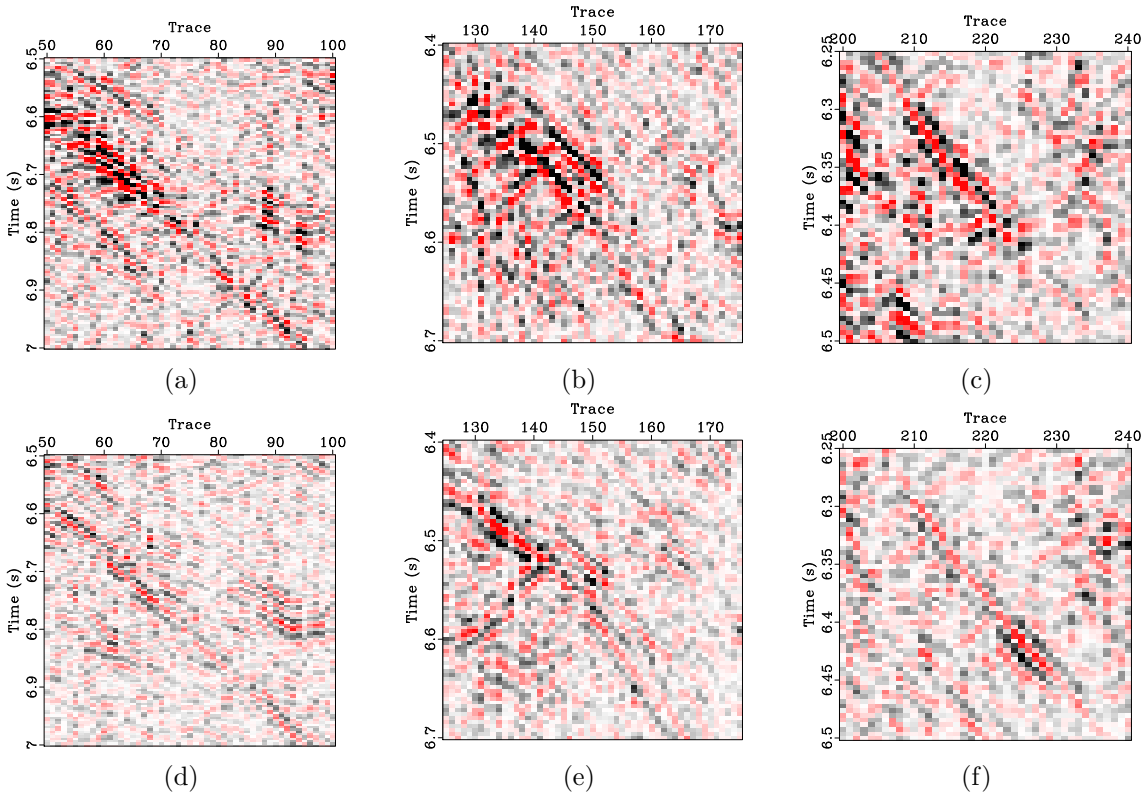

Figure 13: Zoomed comparison of the diffraction image. Top row: PWD method. Bottom row: LRRA method. (a) and (d) correspond to the frame box A in Figure 11. (b) and (e) correspond to the frame box B in Figure 11. (c) and (f) correspond to the frame box C in Figure 11.

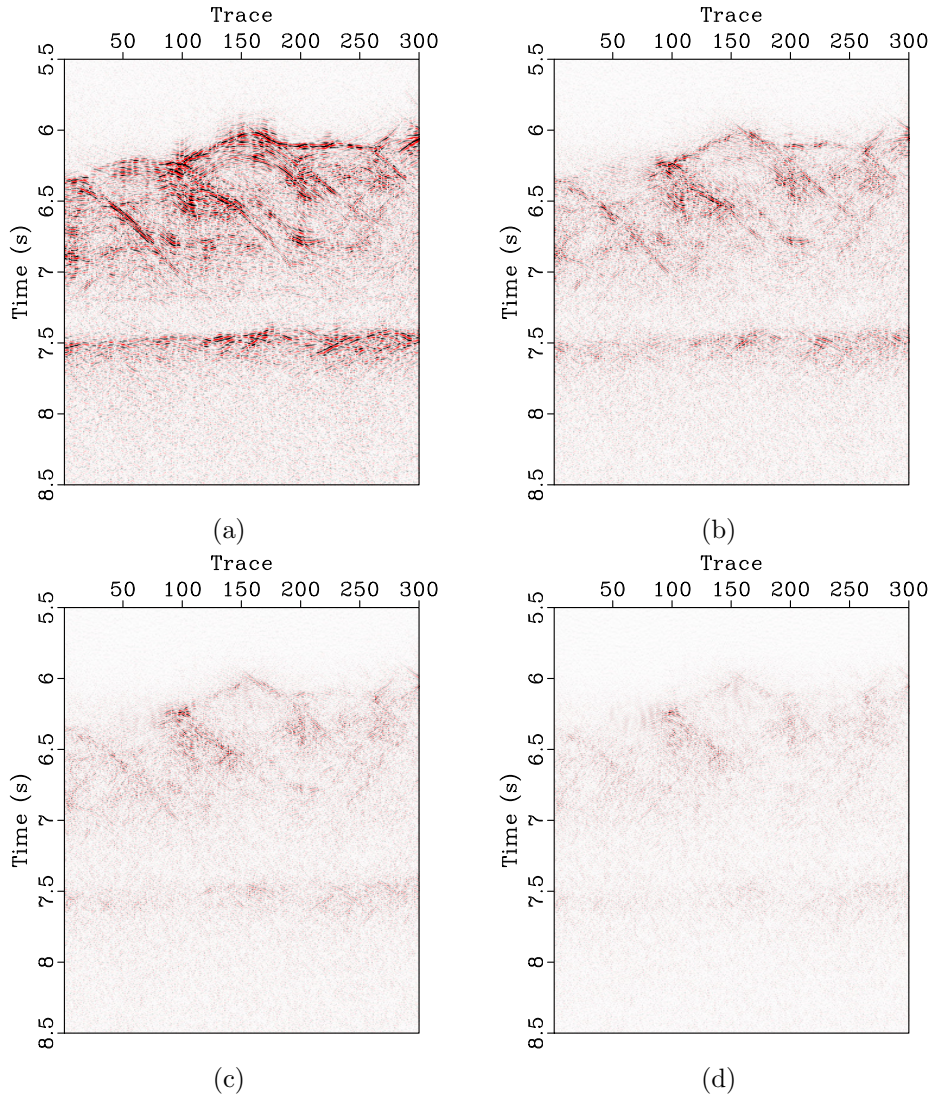

Figure 14: Diffraction images from localized rank-reduction method by manually chosen rank. (a) N=1. (b) N=2. (c) N=3. (d) N=4.

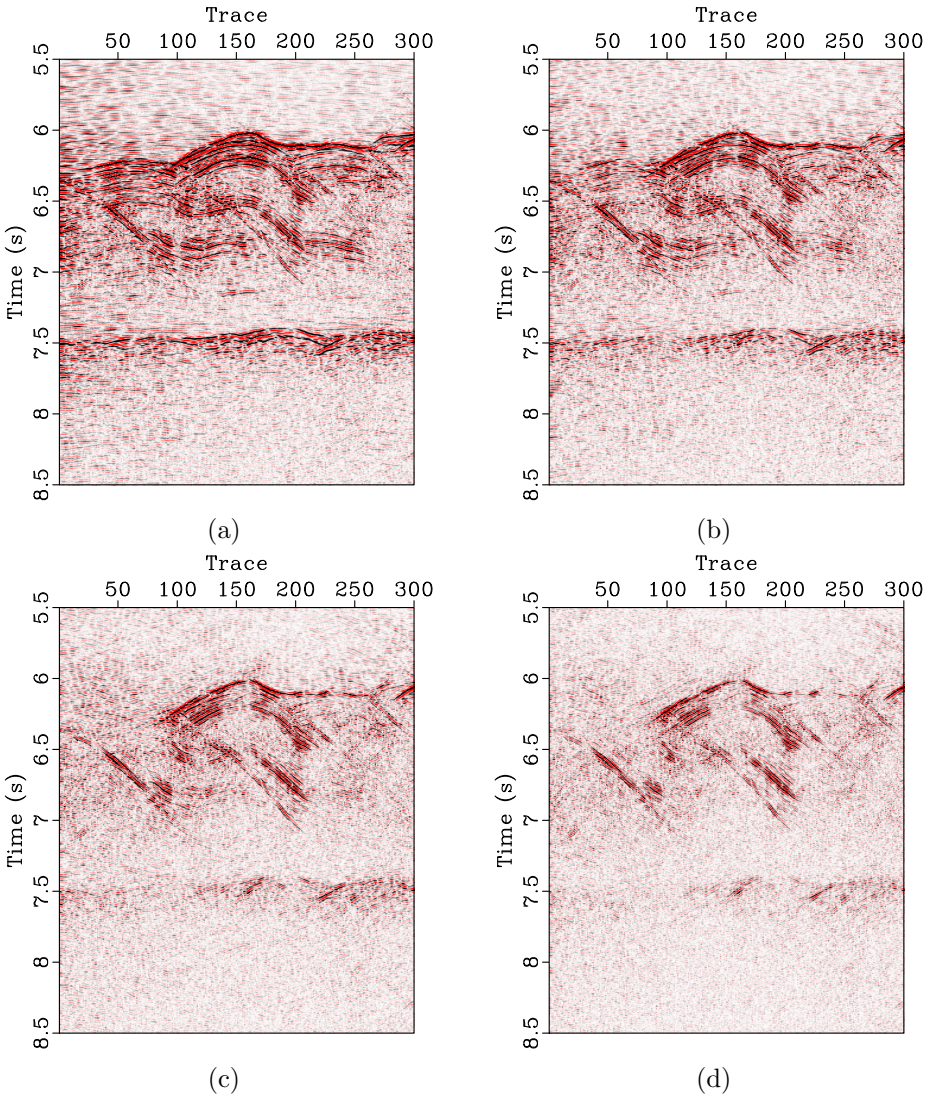

Figure 15: Diffraction images using global rank-reduction method with N=5 (a), N=10 (b), N=20 (c), and N=30 (d).

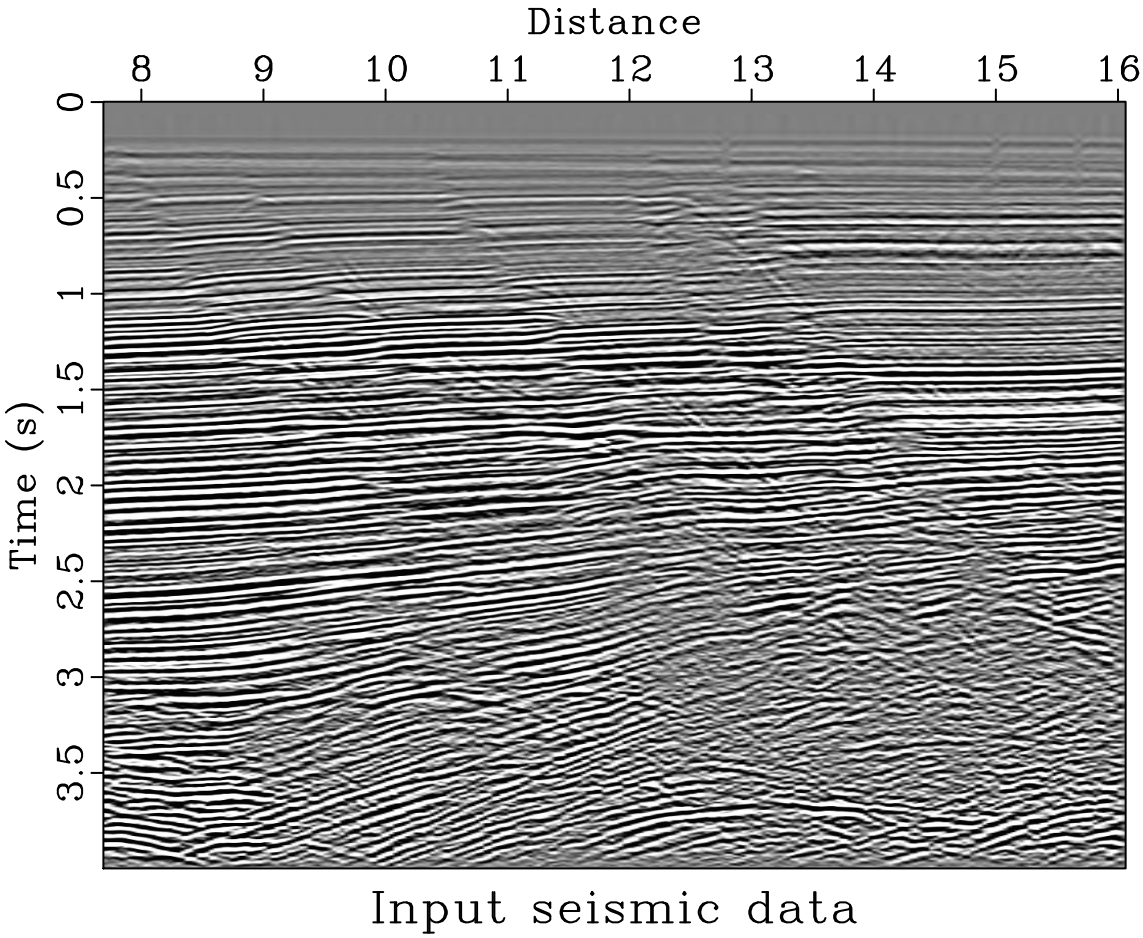

Figure 16: Input marine seismic data.

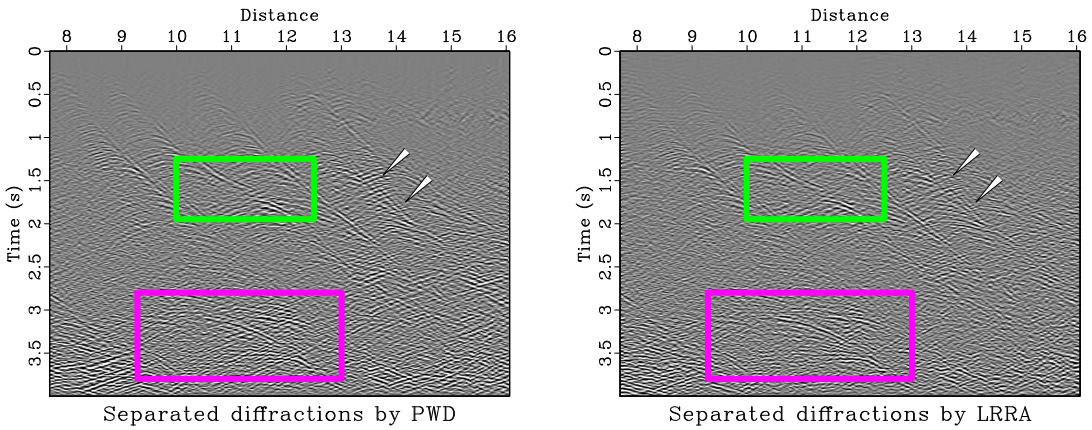

Figure 17: (a) Separated diffractions by PWD. (b) Separated diffractions by LRRA. Note that the PWD method causes more leaked reflection energy as highlighted by the frame boxes and labels.

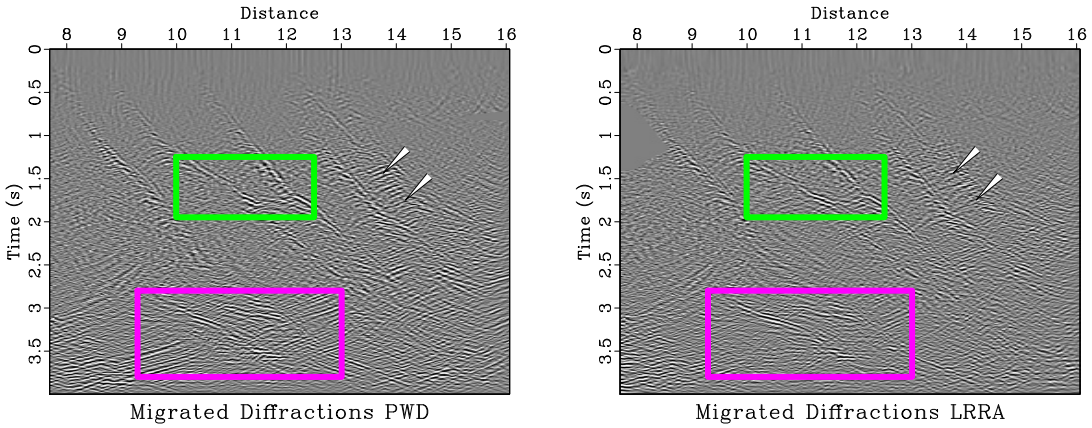

(a) (b)

Figure 18: (a) Migrated image using separated diffractions by PWD. (b) Migrated image using separated diffractions by LRRA. Note the less reflection structure and higher resolution obtained from the LRRA method compared with the PWD method.

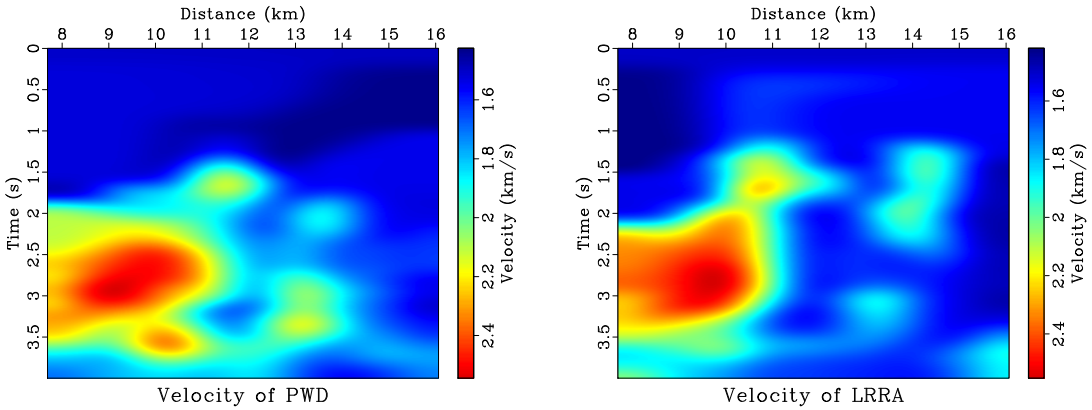

(a) (b)

Figure 19: (a) Picked velocity profile from separated diffractions by PWD. (b) Picked velocity profile from separated diffractions by LRRA.

localized rank-reduction method are accurate both kinematically and dynamically. Synthetic and field examples demonstrate the effectiveness of the proposed method in diffraction separation and further in imaging of the separated diffractions.

ACKNOWLEDGEMENTS

The research is supported by the Starting Funds from Zhejiang University.

DATA AND MATERIALS AVAILABILITY

Data associated with this research are available and can be obtained by contacting the corresponding author.

REFERENCES

Asgedom, E. G., L. J. Gelius, and M. Tygel, 2013, 2D common-offset traveltime based diffraction enhancement and imaging: Geophysical Prospecting, **61**, 1178–1193.

Bakhtiari Rad, P., B. Schwarz, D. Gajewski, and C. Vanelle, 2018, Common-reflection-surface-based prestack diffraction separation and imaging: Geophysics, **83**, no. 1, S47–S55.

Berkovitch, A., I. Belfer, Y. Hassin, and E. Landa, 2009, Diffraction imaging by multifocusing: Geophysics, **74**, no. 6, WCA75–WCA81.

Chen, Y., M. Bai, and Y. Chen, 2019, Obtaining free USArray data by multi-dimensional seismic reconstruction: Nature Communications, **10**, no. 1, 4434.

Chen, Y., H. Chen, K. Xiang, and X. Chen, 2017, Preserving the discontinuities in least-squares reverse time migration of simultaneous-source data: Geophysics, **82**, no. 3, S185–S196.

Chen, Y., D. Zhang, Z. Jin, X. Chen, S. Zu, W. Huang, and S. Gan, 2016, Simultaneous denoising and reconstruction of 5-D seismic data via damped rank-reduction method: Geophysical Journal International, **206**, no. 3, 1695 – 1717.

Coimbra, T. A., J. H. Faccipieri, J. H. Speglich, L.-J. Gelius, and M. Tygel, 2018, Enhancement of diffractions in prestack domain by means of a finite-offset double-square-root traveltime: Geophysics, **84**, no. 1, V81–V96.

Decker, L., D. Merzlikin, and S. Fomel, 2017, Diffraction imaging and time-migration velocity analysis using oriented velocity continuation: Geophysics, **82**, no. 2, U25–U35.

Dell, S., and D. Gajewski, 2011, Common-reflection-surface-based workflow for diffraction imaging: Geophysics, **76**, no. 5, S187–S195.

Ekstrom, M. P., 1996, Dispersion estimation from borehole acoustic arrays using a modified matrix pencil algorithm: Conference Record of the Twenty-Ninth Asilomar Conference on Signals, Systems and Computers, IEEE, 449–453.

Fomel, S., 2002a, Antialiasing of Kirchhoff operators by reciprocal parameterization: Journal of Seismic Exploration, **10**, 293–310.

———, 2002b, Application of plane-wave destruction filters: Geophysics, **67**, no. 6, 1946–1960.

———, 2003, Velocity continuation and the anatomy of residual prestack time migration: Geophysics, **68**, no. 1, 1650–1661.

Fomel, S., E. Landa, and M. T. Taner, 2007, Post-stack velocity analysis by separation and imaging of seismic diffractions: Geophysics, **72**, no. 6, U89–U94.

Gelius, L. J., 1995, Limited-view diffraction tomography in a nonuniform background: Geophysics, **60**, no. 2, 580–588.

Hua, Y., and T. K. Sarkar, 1991, On svd for estimating generalized eigenvalues of singular matrix pencil in noise: 1991., IEEE International Sympoisum on Circuits and Systems, IEEE, 2780–2783.

Huang, W., R. Wang, Y. Chen, H. Li, and S. Gan, 2016, Damped multichannel singular spectrum analysis for 3D random noise attenuation: Geophysics, **81**, no. 4, V261–V270.

Jain, V., 1974, Filter analysis by use of pencil of functions: Part i: IEEE Transactions on Circuits and Systems, **21**, 574–579.

Kanasewich, E. R., and S. M. Phadke, 1988, Imaging discontinuities on seismic sections: Geophysics, **53**, no. 3, 334–345.

Klokov, A., and S. Fomel, 2012, Separation and imaging of seismic diffractions using migrated dip-angle gathers: Geophysics, **77**, S131–S143.

Landa, E., and S. Keydar, 1998, Seismic monitoring of diffraction images for detection of local heterogeneities: Geophysics, **63**, no. 3, 1093–1100.

Lang, S., A. Kurkjian, J. McClellan, C. Morris, and T. Parks, 1987, Estimating slowness dispersion from arrays of sonic logging waveforms: Geophysics, **52**, no. 4, 530–544.

Li, Z., and J. Zhang, 2019, 3D diffraction imaging with Kirchhoff time migration using vertical traveltime difference gathers: Geophysics, **84**, no. 6, S555–S566.

Lin, P., S. Peng, J. Zhao, and X. Cui, 2020, Diffraction separation and imaging using multichannel singular-spectrum analysis: Geophysics, **85**, no. 1, V11–V24.

Liu, L., E. Vincent, X. Ji, F. Qin, and Y. Luo, 2016, Imaging diffractors using wave-equation migration: Geophysics, **81**, no. 6, S459–S468.

Merzlikin, D., S. Fomel, and M. K. Sen, 2019, Least-squares path-summation diffraction imaging using sparsity constraints: Geophysics, **84**, no. 3, S187–S200.

Oropeza, V., and M. Sacchi, 2011, Simultaneous seismic data denoising and reconstruction via multichannel singular spectrum analysis: Geophysics, **76**, no. 3, V25–V32.

Protasov, M., K. Gadylshin, V. Tcheverda, and A. Pravduhin, 2019, 3D diffraction imaging of fault and fracture zones via image spectral decomposition of partial images: Geophysical Prospecting, **67**, 1256–1270.

Santos, L. A., W. J. Mansur, and G. A. McMechan, 2012, Tomography of diffraction-based focusing operators: Geophysics, **77**, no. 5, R217–R225.

Sarkar, T. K., and O. Pereira, 1995, Using the matrix pencil method to estimate the parameters of a sum of complex exponentials: IEEE Antennas and Propagation Magazine, **37**, 48–55.

Sava, P. C., B. Biondi, and J. Etgen, 2005, Wave-equation migration velocity analysis

by focusing diffractions and reflections: Geophysics, **70**, no. 3, U19–U27.

Schwarz, B., 2019, Coherent wavefield subtraction for diffraction separation: Geophysics, **84**, no. 3, V157–V168.

Siahsar, M. A. N., S. Gholtashi, E. Olyaei, W. Chen, and Y. Chen, 2017, Simultaneous denoising and interpolation of 3D seismic data via damped data-driven optimal singular value shrinkage: IEEE Geoscience and Remote Sensing Letters, **14**, no. 7, 1086–1090.

Tschannen, V., N. Ettrich, M. Delescluse, and J. Keuper, 2020, Detection of point scatterers using diffraction imaging and deep learning: Geophysical Prospecting, **68**, 830–844.

Vicente, O., and S. Mauricio, 2011, Simultaneous seismic data denoising and reconstruction via multichannel singular spectrum analysis: Geophysics, **76**, no. 3, V25–V32.

Waheed, U. b., T. Alkhalifah, and A. Stovas, 2013, Diffraction traveltime approximation for TI media with an inhomogeneous background: Geophysics, **78**, no. 5, WC103–WC111.

Yuan, H., M. Montazeri, M. C. Looms, and L. Nielsen, 2019, Diffraction imaging of ground-penetrating radar data: Geophysics, **84**, no. 3, H1–H12.

Zhang, D., T. W. Fei, C. Tsingas, and Y. Luo, 2019, Efficient wave-equation-based diffraction imaging: Geophysics, **84**, no. 5, S389–S399.

Zhang, J., and J. Zhang, 2014, Diffraction imaging using shot and opening-angle gathers: A prestack time migration approach: Geophysics, **79**, no. 2, S23–S33.

Zhou, B., P. Hatherly, and W. Sun, 2017, Enhancing the detection of small coal structures by seismic diffraction imaging: International Journal of Coal Geology, **178**, 1–12.

Zhou, B., and W. Sun, 2018, Seismic diffraction imaging for improved coal structure detection in complex geological environments: ASEG Extended Abstracts, **2018**, 1–5.

Zu, S., H. Zhou, W. Mao, D. Zhang, C. Li, X. Pan, and Y. Chen, 2017, Iterative deblending of simultaneous-source data using a coherency-pass shaping operator: Geophysical Journal International, **211**, no. 1, 541–557.